

Subpicosecond laser ablation behavior of a magnesium target and crater evolution: Molecular dynamics study and experimental validation

Guolong Jiang(江国龙) and Xia Zhou(周霞)

Citation: Chin. Phys. B, 2024, 33 (**7**): 077901. DOI: 10.1088/1674-1056/ad3ef8
Journal homepage: http://cpb.iphy.ac.cn; http://iopscience.iop.org/cpb

What follows is a list of articles you may be interested in

Laser fragmentation in liquid synthesis of novel palladium-sulfur compound nanoparticles as efficient electrocatalysts for hydrogen evolution reaction

Guo-Shuai Fu(付国帅), Hong-Zhi Gao(高宏志), Guo-Wei Yang(杨国伟), Peng Yu(于鹏), and Pu Liu(刘璞)
Chin. Phys. B, 2022, 31 (**7**): 077901. DOI: 10.1088/1674-1056/ac4e0e

Time-dependent photothermal characterization on damage of fused silica induced by pulsed 355-nm laser with high repetition rate

Chun-Yan Yan(闫春燕), Bao-An Liu(刘宝安), Xiang-Cao Li(李香草), Chang Liu(刘畅), Xin Ju(巨新)
Chin. Phys. B, 2020, 29 (**2**): 027901. DOI: 10.1088/1674-1056/ab671d

Time-resolved shadowgraphs and morphology analyses of aluminum ablation with multiple femtosecond laser pulses

Zehua Wu(吴泽华), Nan Zhang(张楠), Xiaonong Zhu(朱晓农), Liqun An(安力群), Gangzhi Wang(王刚志), Ming Tan(谭明)
Chin. Phys. B, 2018, 27 (**7**): 077901. DOI: 10.1088/1674-1056/27/7/077901

Self-organized voids revisited： Experimental verification of the formation mechanism

Song Juan (宋娟), Ye Jun-Yi (叶俊毅), Qian Meng-Di (钱梦迪), Luo Fang-Fang (骆芳芳), Lin Xian (林贤), Bian Hua-Dong (卞华栋), Dai Ye (戴晔), Ma Guo-Hong (马国宏), Chen Qing-Xi (陈庆希), Jiang Yan (姜燕), Zhao Quan-Zhong (赵全忠), Qiu Jian-Rong (邱建荣)
Chin. Phys. B, 2014, 23 (**7**): 077901. DOI: 10.1088/1674-1056/23/7/077901

Suppressing the mechanical quadrature error of a quartz double-H gyroscope through laser trimming

Zhao Ke (赵克), Feng Li-Hui (冯立辉), Wang Qian-Qian (王茜蒨), Liu Ming-Zhi (刘明智), Wang Ben-Guo (王本国), Cui Fang (崔芳), Sun Yu-Nan (孙雨南)
Chin. Phys. B, 2013, 22 (**11**): 117901. DOI: 10.1088/1674-1056/22/11/117901

Subpicosecond laser ablation behavior of a magnesium target and crater evolution: Molecular dynamics study and experimental validation

Guolong Jiang(江国龙) and Xia Zhou(周霞)†

State Key Laboratory of Structural Analysis for Industrial Equipment, Department of Engineering Mechanics, Faculty of Vehicle Engineering and Mechanics, Dalian University of Technology, Dalian 116024, *China*

(Received 20 January 2024; revised manuscript received 29 March 2024; accepted manuscript online 16 April 2024)

The micro-ablation processes and morphological evolution of ablative craters on single-crystal magnesium under subpicosecond laser irradiation are investigated using molecular dynamics (MD) simulations and experiments. The simulation results exhibit that the main failure mode of single-crystal Mg film irradiated by a low fluence and long pulse width laser is the ejection of surface atoms, which has laser-induced high stress. However, under high fluence and short pulse width laser irradiation, the main damage mechanism is nucleation fracture caused by stress wave reflection and superposition at the bottom of the film. In addition, Mg$[0\,0\,0\,1]$ has higher pressure sensitivity and is more prone to ablation than Mg$[1\,0\,\bar{1}\,0]$. The evolution equation of crater depth is established using multi-pulse laser ablation simulation and verified by experiments. The results show that, under multiple pulsed laser irradiation, not only does the crater depth increase linearly with the pulse number, but also the quadratic term and constant term of the fitted crater profile curve increase linearly.

Keywords: laser-material interaction, molecular dynamics (MD) simulation, ablation crater morphology, magnesium

PACS: 79.20.Eb, 79.20.Ds, 81.15.Fg **DOI:** 10.1088/1674-1056/ad3ef8

1. Introduction

Short-pulse laser ablation of metal materials is a core technology in engineering applications, such as high-precision cutting, drilling, and the fabrication of nano-functional and nano-bionic structures.[1–3] Currently, research on the mechanisms of laser ablation of materials has yielded significant results.[4–7] The response of metal materials to laser irradiation is complex and includes electron excitation through photon absorption, transient modification of metal physical properties, relaxation of laser-induced stresses, non-equilibrium phase transformations, plasma formation and shielding phenomena. Numerical simulations, especially molecular simulation, have made a significant contribution to the discovery of these phenomena. Methods of molecular simulation for studying the interaction between lasers and metals include molecular mechanics (MM), the Monte Carlo (MC) method, and molecular dynamics (MD). Since the last method can provide more deterministic results compared to the first two methods and the simulated results are closer to the actual microstate of the system, MD has been widely used in recent years. In the field of laser simulation, Zhigilei[8] proposed the MD method coupled with a two-temperature model (TTM-MD) to fully reveal the behavior of atoms on the nanoscale when irradiated by an ultrashort pulse laser. However, when the laser pulse width exceeds the characteristic times of photoinduced electronic processes, especially in the subpicosecond range, it is not necessary to specifically consider the electron–lattice interaction effects. It is reasonable to use a more universal and simpler one-temperature model.[9–11]

Due to their high strength-to-weight ratio and superior damping and cutting properties, magnesium and its alloys have broad application prospects in the machining of precision components and composite substrates.[12–14] Combined with laser machining technology, magnesium products have the potential to become the next generation core components of large equipment. Therefore, it is necessary to quantitatively analyze the mechanism of magnesium ablation under laser irradiation and summarize the evolutionary law of ablation crater morphology under multi-pulse laser conditions.[15,16] Yayoglu *et al.*[16] conducted experiments to study the effects of picosecond laser parameters on the surface of a high-purity magnesium target, and obtained the evolutionary law of the ablation crater section under repeated laser irradiation. They suggested that increasing the number of repetitions is preferable to increasing the average laser power in order to achieve deeper grooves.

Based on the above achievements, this work provides a detailed characterization of the thermodynamic behavior of single-crystal magnesium film irradiated by a laser with different pulse widths and fluences, and the effects of the spatial relationship between the crystal direction and the laser incident direction are considered. Additionally, the study reveals the ablation mechanisms of magnesium at various laser fluences and estimates the penetration thresholds for the ablation

†Corresponding author. E-mail: zhouxia@dlut.edu.cn

© 2024 Chinese Physical Society and IOP Publishing Ltd

of single-crystal magnesium films. The study demonstrates that ablation occurs through two primary failure modes: laser-induced phase explosion of surface atoms, which is supported by snapshots of the temperature field showing the separation of high-temperature atoms; and structural fracture resulting from stress wave reflection and superposition, which is illustrated by snapshots of the stress state of atoms, depicting the transfer of stress waves during ablation. Moreover, molecular dynamics (MD) simulation was conducted to investigate the multi-pulse laser ablation of single-crystal magnesium. The simulation utilized a bulk atomic structure with a newly modified pressure transmission boundary. Additionally, a laser ablation experiment was performed to examine the evolution law of ablation crater morphology for comparison. By combining the simulation and experimental results, similar but more specific conclusions are drawn compared to the relevant reference. Furthermore, the findings of this study can provide guidance for laser ablation processes and the design of more intricate or refined microstructures on magnesium. This has important significance for the precision processing of magnesium-based materials, such as cutting, drilling, preparation of nanostructures and bionic structures. It also has reference significance for laser protection of magnesium-based components.

2. Calculation model

2.1. Atomic model of laser ablation on Mg films with consideration of plasma plume shielding effect

MD simulations of laser ablation on Mg targets were carried out using LAMMPS[17] software in this work. The embedded-atom-method (EAM) developed by Sun *et al.*[18] is used here to describe the interaction between magnesium atoms. The total potential energy $E_{\rm tot}$ is composed of a pairwise and a many-body embedding part and is given by

$$E_{\rm tot} = \sum_{i=1}^{N-1} \sum_{j=i+1}^{N} \phi(r_{ij}) + \sum_{i=1}^{N} F(\rho_i), \tag{1}$$

where r_{ij} represents the distance between atoms i and j, and F is the embedding energy. Here, ρ_i is dependent on the distance between the atom i and other atoms, which can be expressed as $\rho_i = \sum_{j\neq i} \varphi(r_{ij})$, and a detailed explanation of the function $\phi(r_{ij})$, $F(\rho)$, $\varphi(r_{ij})$ can be found in reference.[17]

In the simulation of ablation on thin Mg films, hexagonal close-packed (HCP) Mg single crystals were placed in a rectangular coordinate system. To demonstrate the temperature change and stress distribution in the Mg target with different crystal orientations during the laser–Mg interaction, two different Mg models with laser beams along Mg$[0\,0\,0\,1]$ and Mg$[1\,0\,\bar{1}\,0]$, respectively, are established. Both models use periodic boundary conditions in the X and Y directions and have dimensions of 27.71 Å×32.00 Å. The laser beam is always parallel to the z-axis, and a free boundary condition is applied in this direction. In the two models, the spatial relationship between the crystal direction and the coordinate axis is as follows: the X, Y, and Z axes along with the crystal orientations of $[2\bar{1}\,1\,0]$, $[1\,1\,2\,0]$ and $[0\,0\,0\,1]$ in the Mg$[0\,0\,0\,1]$ model and the X, Y, and Z axes along with the crystal orientation of the $[1\,2\,\bar{1}\,0]$, $[0\,0\,0\,1]$ and $[1\,0\,\bar{1}\,0]$ in the Mg$[1\,0\,\bar{1}\,0]$ model. Both models have a length of 100 nm and consist of 38000 and 36960 atoms, respectively. Detailed information about the models is provided in Fig. 1.

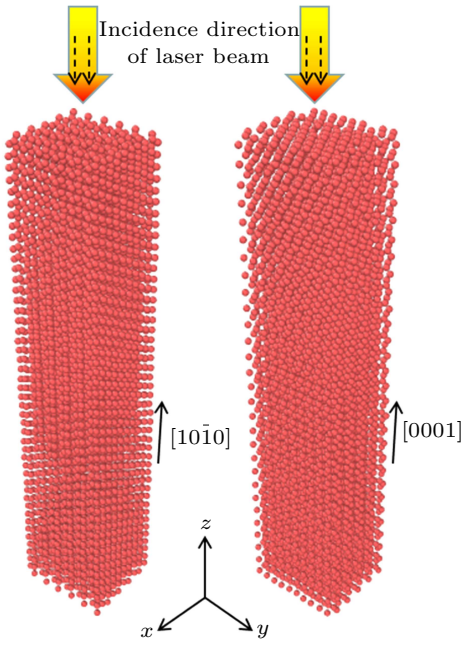


Fig. 1. The spatial relationship between crystal orientation and the laser.

A three-dimensional code is presented before the MD simulation for the laser deposition processes on metal, which is mainly used to describe the instantaneous phenomenon of a laser irradiating on a metal surface and energizing the atom at different position. The energy absorbed by each magnesium atom can be expressed as

$$S(x_i,y_i,z_i) = (1-R)\left[I_0 \mathrm{e}^{(-lz)}\right] \times \left\{\frac{a_c^2}{8\pi r_b^2}\exp\left[-\frac{a_c^2}{8r_b^2}(x_i^2+y_i^2)\right]\right\}. \tag{2}$$

In our simulation, the laser is set as an ultraviolet pulsed laser with a wavelength of 355 nm; the reflectivity (R) and penetration depth (l) are 0.779 and 18.2 nm in the Mg$[0\,0\,0\,1]$ model and 0.855 and 16.45 nm in the Mg$[1\,0\,\bar{1}\,0]$ model.[19] In addition, three different pulse widths (60 fs, 600 fs and 6 ps) and six incremental laser fluences from 50 mJ/cm^2 to 300 mJ/cm^2 are involved in the MD simulations to study the laser ablation of Mg films. Over the duration of the laser pulse, the photon density irradiated by the laser follows a Gaussian distribution.

When the laser pulse width exceeds the characteristic times of photoinduced electronic processes, the shielding effect of the plasma plume must be considered. During laser irradiation, a plasma plume is produced above the surface of the target. And with the energy absorption of plasma, the energy reaching the material surface is not equal to the beam energy originally emitted by the laser device. It is assumed that the energy E_a is absorbed instantly and equally by the plasma. The increase in plasma temperature ΔT is given by[20]

$$\Delta T = \frac{(\gamma-1)E_a}{kN} = \frac{(\gamma-1)mE_a}{k\Delta z\rho}, \tag{3}$$

where γ is the effective adiabatic coefficient, and k and N represent the Boltzmann constant and the number of atoms that are vaporized, respectively. Here, N can be calculated by the mass of a single atom m and mass density ρ.

In the simulation, the pulse laser with energy fluence I_0 is incident along the z-axis and perpendicular to the metal surface. The residual radiation energy after passing through the plasma is

$$I(t) = I_0(t)\exp\left[\Lambda(t)\right] = I_0(t)\exp\left[-\int_0^{\infty}\alpha(n,T)\,\mathrm{d}z\right], \tag{4}$$

where $\Lambda(t)$ represents the equivalent optical thickness of the plasma plume. Here, α is the function of plasma temperature $T = T(z,t)$ and the atomic number density $n = n(z,t)$ of the particles. The plasma shielding effect is great when the laser pulse width is large, and consideration of plasma shielding will reduce the peak temperature of the target by 4–6 times during the simulation.[5] In this study, the plasma shielding effect is considered at 600 fs and 6 ps laser pulses, but not at 60 fs laser pulses as the shielding effect has not formed and the pulse has ended.

2.2. Simulation of crater morphology evolution with virtual stress transfer boundary

To investigate the morphological evolution of ablative craters under multi-pulse laser irradiation, an approximate approach is used in this study. As shown in Fig. 2, the representation of the laser-induced crater morphology at the scale of the entire laser spot is based on the concatenation of various block elements. Simulation at the atomic scale is only required at each pixel position. The energy distribution in the spot is axisymmetric, and four points from the center to the edge of the laser spot are selected as pixel positions in this study. The energy fluence at each position is calculated according to the laser energy distribution formula. The position and energy information is provided in Table 1.

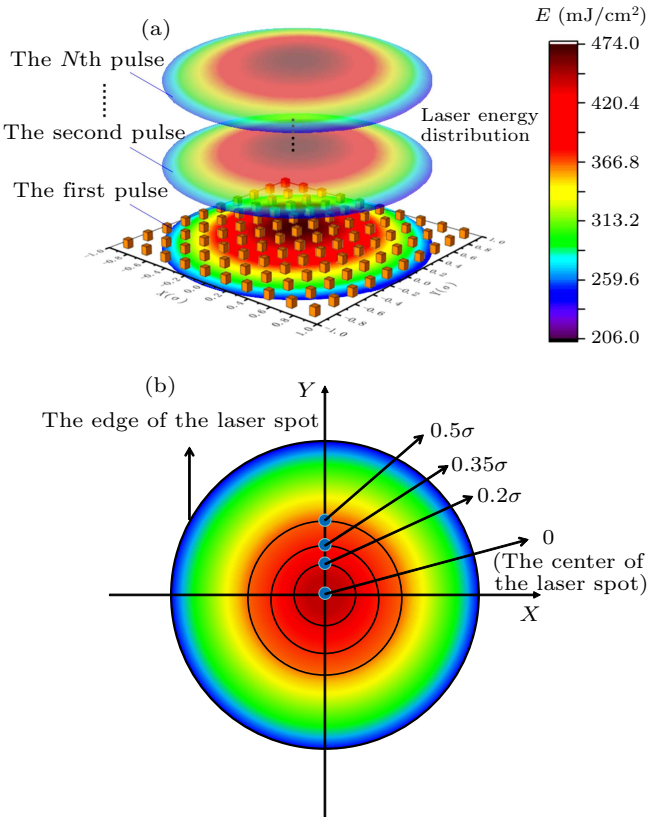


Fig. 2. Diagrams of (a) multi-pulse laser irradiation and (b) energy distribution in a laser spot. In the simulation process, four reference points within the radius of the spot were selected to perform the multi-pulse ablation calculation.

Table 1. Details of point position distribution.

Model number	ML-1	ML-2	ML-3	ML-4
Distance from laser spot center (σ)	0.5	0.35	0.2	0
Energy fluence (mJ/cm^2)	239.4	328.6	409.1	473.5

Unlike the ablation of metal films, the reflection of stress waves at the bottom boundary of the bulk target should be avoided. Reference [21] established a pressure-transmitting boundary by modifying the atomic states in the boundary region to reduce the intensity of the stress wave reflection. Atoms in the boundary zone experience a total force and can be expressed as

$$F_{bc} = F_0 + \alpha u, \tag{5}$$

where F_0 is a static contribution. The second part is a force which is added externally and is proportional to the velocity u of the atoms in the boundary. The proportionality constant $\alpha = ZA = mn_0c_0A$. On this basis, an improved virtual boundary is added in this study. The virtual boundary scale in the dimension of non-stress wave transmission is consistent with that of the computational domain. The length of the virtual boundary in the stress wave transmission dimension is calculated as follows:

$$L_{BC} \geq \lambda_p = 2\sqrt{E/\rho}\cdot\tau, \tag{6}$$

where λ_p represents the wavelength of the stress wave. Here, E and ρ are the elastic modulus and density of the target material, respectively, and τ is the pulse width of the laser. The time required for the stress wave to reach the virtual boundary can be calculated as follows:

$$t_c = (L + L_{BC})/c_0. \tag{7}$$

To completely suppress the influence of stress wave reflection on the calculation domain, an external force field is applied to eliminate the stress wave when it reaches the virtual domain based on the simulation result. After the stress control is completed in the virtual domain, the interaction between the virtual domain and the computational domain is terminated in the subsequent computation.

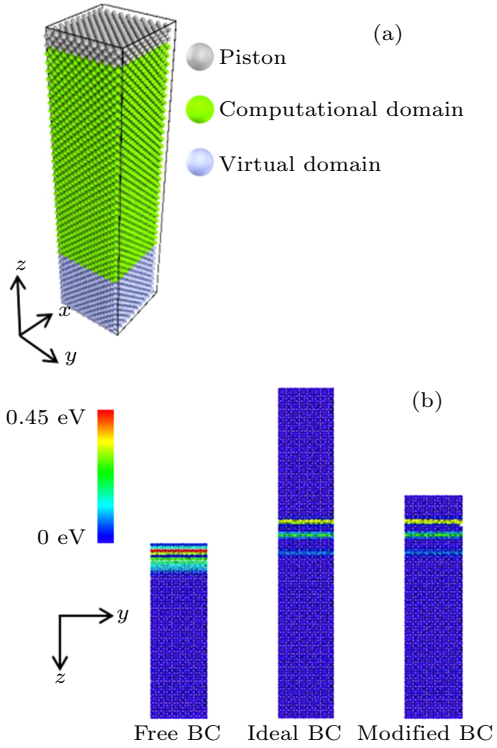


Fig. 3. (a) A schematic diagram of the shock model; (b) the distribution of kinetic energy under different boundary conditions. The reflection and superposition of stress waves appear at the end of the free boundary, which cannot be used in the calculation of semi-infinite models. The ideal model represents an ideal semi-infinite model that is too large and still has a terminal. The virtual boundary model has a length close to that of the free boundary model, and the state of the stress wave when it reaches the boundary is consistent with the ideal boundary.

To validate the effectiveness of the modified boundary, three atomic models of single-crystal Cu, similar to the model in reference,[21] were constructed. The free boundary model is characterized by an unconstrained bottom boundary. The ideal boundary model is an extended model without a bottom boundary, and the pressure wave can continue to travel. The modified boundary model incorporates a virtual boundary, the length of which is calculated using Eq. (6) in the bottom boundary region. The stress wave load is implemented using the momentum mirror method, which involves setting a piston to hit the calculation region.

The dimensions of the models with a free boundary, ideal boundary, and modified boundary are $10 \times 10 \times 32a$, $10 \times 10 \times 62a$ and $10 \times 10 \times 42a$, respectively. Figure 3 shows a schematic diagram of the shock model and the distribution of kinetic energy under different boundary conditions when the stress wave reaches the $30a$ region from the loading end. For comparison, only the energy in the first $30a$ region of the three models was considered.

As shown in Fig. 4, the first two charts verify the similarity between the validation model and the literature model, and both have similar results at the free and ideal boundaries. The third chart in Fig. 4 illustrates that the modified boundary, which adds a virtual domain, effectively prevents a sudden increase in E_{kin}, E_{pot} and E_{tot}, and the energy evolution of the system is more similar to the ideal boundary. For the multi-pulse simulation model, the length of each pixel region was set to 500 nm, and the virtual boundary length was set to 100 nm, which is significantly larger than the stress wavelength. Additionally, the initial model comprised 230400 atoms.

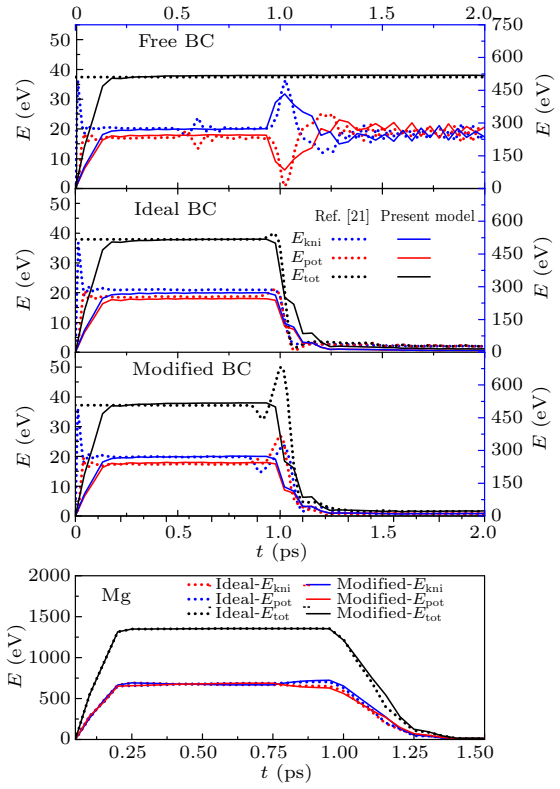


Fig. 4. Energy evolution of a pressure wave traveling through crystallite models with different boundary conditions. The models in the first three graphs are Cu for the comparison between the validation models and the models in reference,[21] and the models in the fourth graph are Mg for the comparison between the modified boundary and the ideal boundary.

Before the MD simulations of laser irradiation, the conjugate gradient method was used to minimize the energy of the initial model and obtain a stable structure. Then, both systems of the above two simulations were completely relaxed

for 50 ps under the isothermal-isobaric (NPT) ensemble with a pressure of 0 bar and a temperature of 300 K. During the relaxation process, the temperature was kept constant at a certain temperature with a Nose–Hoover thermostat and the system press was adjusted using a Parrinello–Rahman barostat. After relaxation, the monocrystalline magnesium model was imported into the external code described above for laser energy deposition. Finally, the computational model was re-imported into LAMMPS for final relaxation. The relaxation process adopted an NVE ensemble, the temperature was set at 300 K, and the relaxation time was 2 ns.

3. Results and discussion

3.1. Mechanisms of photomechanical spallation and the response of Mg films with various crystal orientations to laser irradiation

The ablation morphology of the target with different crystal orientations is shown in Fig. 5. The laser fluence and pulse width are both 150 mJ/cm^2 and 600 fs in both directions. Particle detachment and ejection from the target can be observed in both crystal orientations. Based on the atomic structure at different times, the entire ablation process can be divided into three stages. In the initial stage, the atomic states in both models exhibit similarities. After energy absorption, the kinetic energy of atoms on the target surface increases significantly. These energetic atoms can disrupt stable atomic structures and induce phase transitions on the metal surface. Simultaneously, due to the interaction between adjacent atoms, the kinetic energy of the atoms on the target surface will propagate downward and then reflect back. Therefore, this stage can be defined as the atomic structure destruction stage. The second stage occurs about 10 ps after laser irradiation, with a large number of atoms rapidly separated from the substrate; the atomic states in the two models began to differ. The main observation is that the number and kinetic energy of atoms ejected from Mg[0001] are higher compared to Mg[10$\bar{1}$0]. The final stage is characterized by atomic aggregation and stabilization. At 50 ps after laser irradiation, the scattered atoms agglomerate and condense into nanoclusters. Some of these atoms, which have lost interaction with the underlying substrate, will be ejected from the computational domain, while others will be deposited on the substrate surface due to the attraction of the underlying atoms. This phenomenon is macroscopically characterized by remelting and deposition of nanoparticles on metal surfaces. Due to the larger atomic spacing in the Mg[0001], it is more susceptible to destruction during ablation compared to the Mg[10$\bar{1}$0], resulting in a greater ablation depth for the Mg[0001] substrate.

Figures 6(a) and (b) show the pressure contours in the z-direction of Mg[10$\bar{1}$0] and Mg[0001], respectively, during the ablation process. The energy transfer of high-energy atoms forms a thermoelastic stress wave in the depth direction of the model. This stress wave consists of a compression component (red area in Fig. 6) followed by a tension component (blue area in Fig. 6). As shown in Fig. 6, the peak value of the stress wave generated by 150 mJ/cm^2 lasers is lower than the strength of Mg[10$\bar{1}$0] (6.02 GPa) and higher than the strength of Mg[0001] (3.16 GPa). This is also the main reason that leads to the nucleation growth and eventual fracture of the Mg[0001] model bottom but no obvious change in the Mg[10$\bar{1}$0] model bottom.

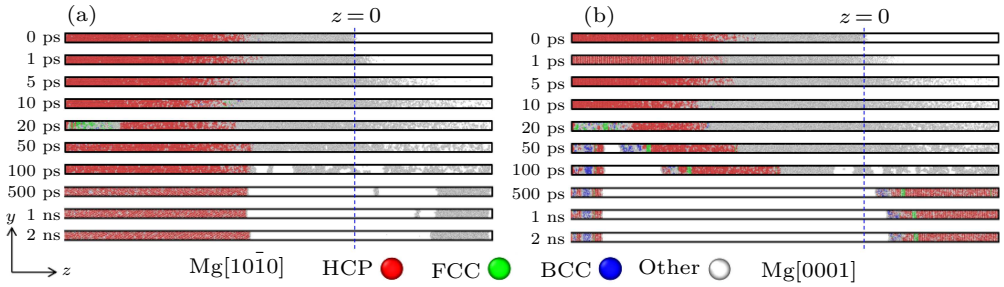


Fig. 5. Atomic structure snapshots of (a) Mg[10$\bar{1}$0] and (b) Mg[0001] during the ablation process.

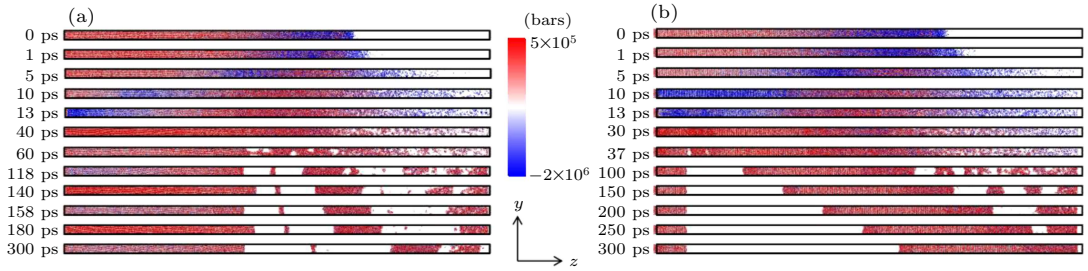


Fig. 6. The z-direction pressure evolution of atoms in the (a) Mg[10$\bar{1}$0] and (b) Mg[0001] systems.

3.2. Effects of laser parameters on Mg ablation response

3.3. Laser pulse width effect

The evolution of atomic structure after irradiation of a laser with different pulse widths is shown in Fig. 7. The final atomic structure demonstrates that the fluence required to penetrate the Mg[0001] substrate under 60 fs and 600 fs laser irradiation is less than 100 mJ/cm^2. However, a 6 ps pulse width laser with the same fluence cannot break down the substrate completely; this is because the laser fluence per unit time decreases with the increase in the pulse width. Basically, the system has more time to complete the energy transfer between atoms and avoids stress concentration.

The pressure and temperature evolution inside the Mg substrate after photon energy deposition is shown in Fig. 8. Obviously, atoms on the surface of the target that absorb a substantial amount of laser energy heat up rapidly and are ejected from the calculation domain under high stress. In the region below the surface, tension waves are generated by the interaction between surface and bottom atoms, and the amplitude of the tension wave increases as the pulse width decreases. As shown in Figs. 8(a) and 8(b), tension waves at high stress levels result in nucleation and penetration at the bottom of the Mg films.

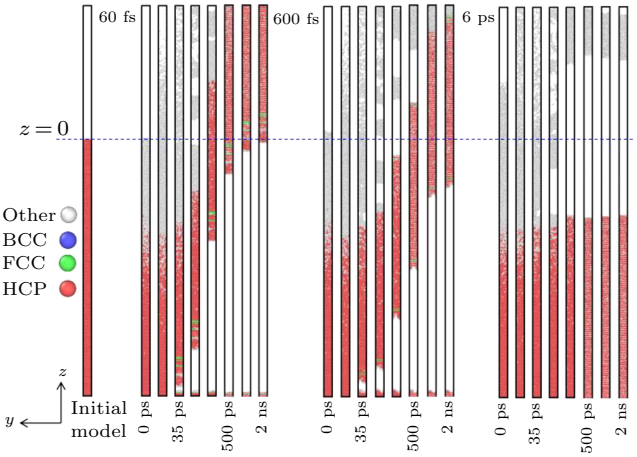


Fig. 7. Atomic structure evolution of the target irradiated by a laser with different pulse widths.

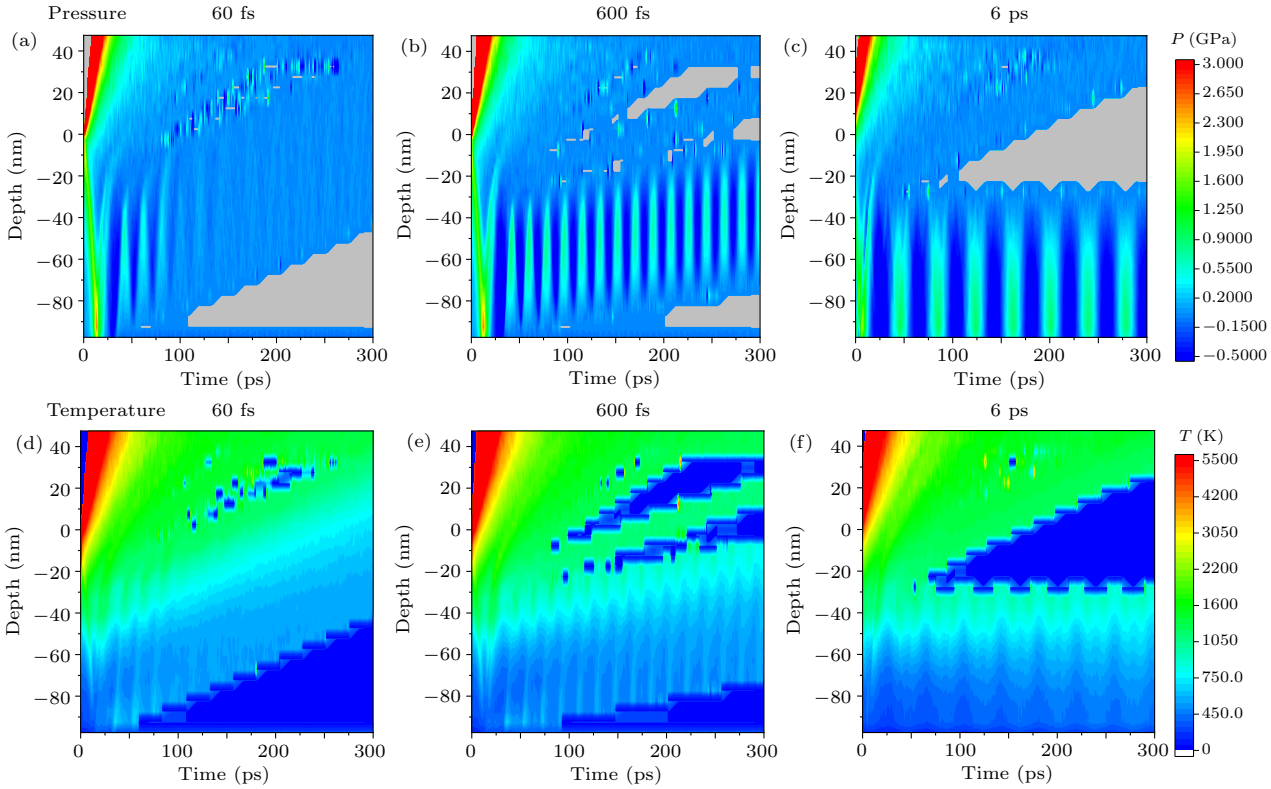


Fig. 8. Internal pressure and temperature evolution of Mg[0001] irradiated by a laser with different pulse widths. Any coordinate position in the figure represents the temperature or pressure at the corresponding time and depth.

3.3.1. Laser energy fluence effect

Figure 9 shows the MD snapshots of the laser ablation process for the Mg[10$\bar{1}$0] substrate under a 6 ps laser with varying fluence. When the laser fluence is below 100 mJ/cm^2, the atoms at the bottom of the target still maintain the HCP structure because the pressure level of the tension wave is not sufficient to destroy the atomic structure. With the increase in laser fluence, the structure of the target is disrupted. This is caused by an increase in pressure at the bottom of the substrate. In addition, more atoms on the top surface absorb laser energy and are ejected from the target surface compared to under low fluence. This phenomenon mainly occurs in the initial stage of ablation. To provide further details, Fig. 10 illustrates the evolution of atomic kinetic energy in the system during the initial stage. Under irradiation with a higher fluence laser, atoms on the surface exhibit higher kinetic en-

ergy. When the laser energy exceeds 250 mJ/cm^2, fracture and separation occur in the bottom region of the target. This indicates that the ablation penetration threshold of Mg[10$\bar{1}$0] is between 200 mJ/cm^2 and 250 mJ/cm^2 under 6 ps laser irradiation.

Figure 11 summarizes the crack initiation time and position of the Mg substrate with two crystal orientations under irradiation of a laser with varying pulse widths and fluences. As shown in the contour graphs, cracks appear earlier and deeper in Mg[0001] than in Mg[10$\bar{1}$0] under laser irradiation with the same parameters. Additionally, both crystal orientations demonstrate that cracks in the substrate occur earlier and deeper under laser irradiation with high fluence and short pulse width compared to under low fluence and long pulse width. Based on Fig. 11, the ablation penetration threshold of the Mg substrate under laser irradiation with different pulse widths can be estimated. This information is crucial for determining laser parameters in the processing of Mg-based components.

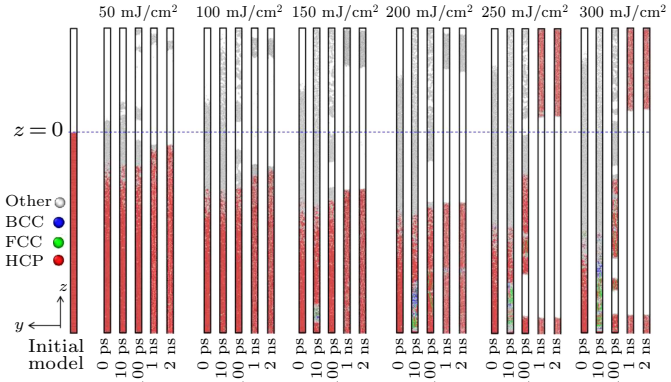


Fig. 9. Atomic structure evolution of the target irradiated by a laser with different fluences.

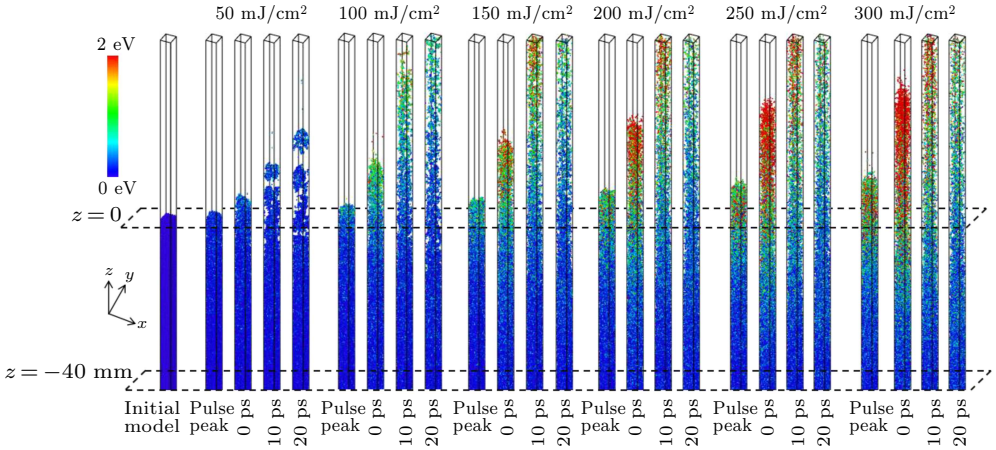


Fig. 10. Kinetic energy evolution of atoms in the system of the Mg target irradiated by a laser with different fluences.

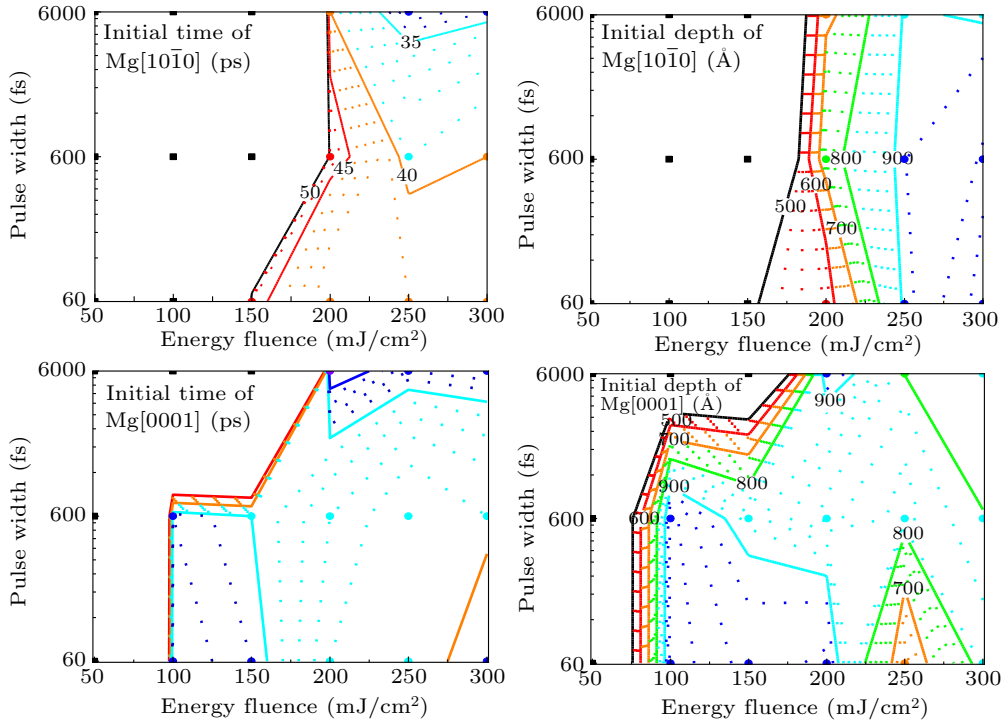


Fig. 11. Contour graphs of crack initiation time and position at the bottom of the substrate under different pulse widths and energy fluences.

3.4. Morphology evolution of crater under multi-pulse laser irradiation and experimental validation

Based on the analysis of the single-pulse laser ablation mechanism of the Mg substrate, this section discusses the ablation crater evolution of the Mg target under multi-pulse laser irradiation via experiment and simulation. The laser parameters in the experiment and simulation are consistent. Each single pulse of the multi-pulse laser has a width of 6 ps and an energy of 300 μJ, and follows a Gaussian distribution in both space and time. In the simulation, an additional code is used to recalibrate the zero surface to achieve full deposition of pulse energy.

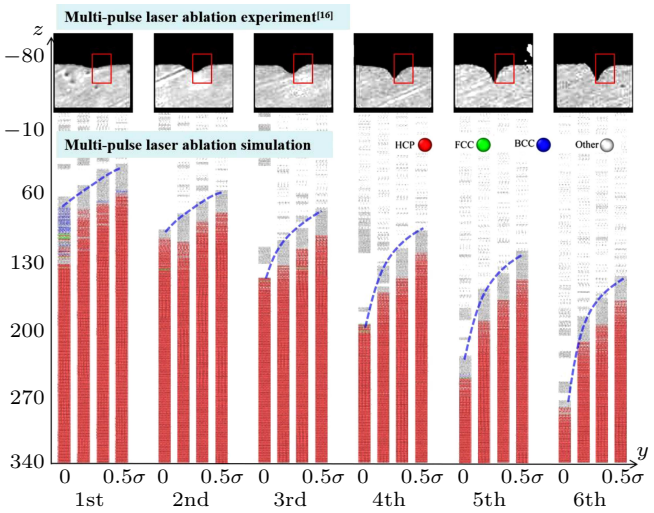


Fig. 12. Atomic structure evolution of the Mg target under irradiation of a multi-pulse laser and validation with the multiple laser ablation experiment in reference.[16]

Figure 12 shows the MD snapshots of atomic structure evolution of the bulk MD model at various distances from the spot center under multi-pulse laser irradiation. The ablation crater profile exhibits a similar evolution pattern to that observed in the multiple laser ablation experiment.[16] The blue dashed line in Fig. 12 demonstrates that the curve from the center to the edge of the ablation crater is approximately parabolic, and the curvature of the parabola changes regularly as the number of laser pulses increases. Similar to the conclusion obtained by the experiment in reference,[16] the trench depths increased almost linearly with the number of laser pulses. Based on this finding, the profile curve of the ablation crater can be expressed as

$$P(n,R) = A(n)R^2 - 2A(n)R + C(n), \tag{8}$$

where $A(n)$ and $C(n)$ are the quadratic coefficient and constant term of the parabola, respectively. To obtain the relationship between the profile curve of the Mg crater and the number of pulses n and the distance from the center R, Fig. 13(a) shows the contour depth fitting curves with different pulse numbers. For comparison, the corresponding Gaussian distribution curve of spot fluence is also included in the figure. Linear regression analysis was then used to calculate the coefficients $A(n)$ and $C(n)$, whose R-squared values are 0.991 and 0.993, respectively in Fig. 13(b). The morphology of the crater profile under multi-pulse laser irradiation will be estimated according to Eq. (8), which can be used as a prediction for practical application of laser ablation machining.

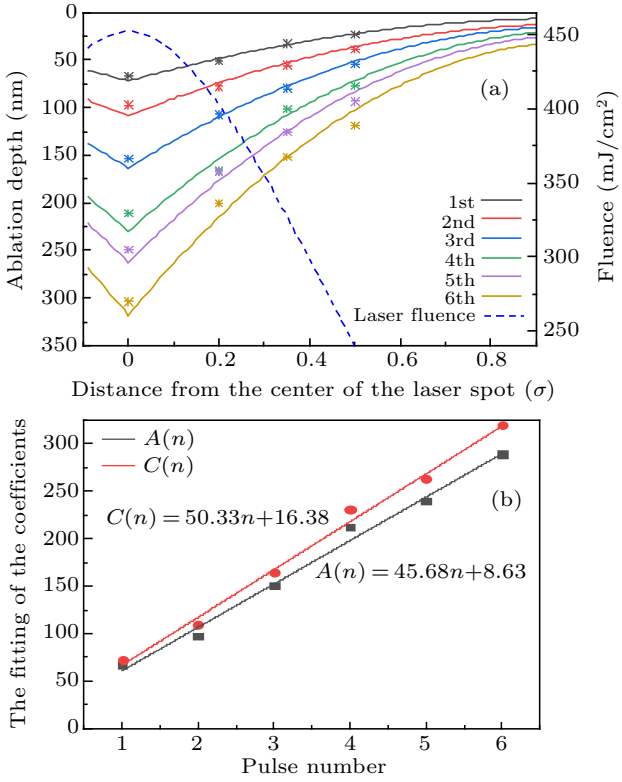


Fig. 13. (a) The fitting curve of the ablation crater profile, and (b) calculation of $A(n)$ and $C(n)$.

MD simulation can provide a more direct demonstration of the entire ablation process compared to experiments. Figure 14 shows the evolution of the temperature field in the system after each pulse of laser irradiation on the target. As seen in the figure, the high-temperature region is primarily located on the surface of the target metal. Additionally, the central region exhibits a larger high-temperature region compared to the edge region, and the phase transition and atomic ejection are more pronounced. Specifically, the liquid phase explosion becomes more violent as the sampling position gets closer to the spot center. At the same time, with the increase in the pulse number, the high-temperature region noticeably shifts downwards. This phenomenon is caused by two factors: one is the increase in ablation depth, and the other is the fact that the disordered atomic structure is more prone to the occurrence of metal bond rupture than the stable HCP structure at the bottom.

The melting point of Mg is 921.95 K. Based on this temperature, contour lines can be drawn in the temperature field (Fig. 14) to analyze the melting depth of the target during the laser ablation process. Figure 15 shows the melting depth and final ablation depth, illustrating the complete evolution

process of crater formation. It is known that phase transition is an inevitable process in ablation crater formation. Consequently, the two depths exhibit a similar evolution process during multi-pulse laser irradiation, although they are not identical. At the first pulse, the melting depth is greater than the final ablation depth across the entire spot range, indicating the presence of liquid residue on the target surface after the initial laser irradiation. Subsequently, with repeated laser irradiation, the melting depth exceeds the final ablation depth at the spot center. This is primarily due to the presence of high-temperature nanoclusters above the target, which reduce the melting-depth calibration accuracy. Meanwhile, the melting depth at the edge of the spot remains greater than the ablation depth. This reflects the fact that a violent non-equilibrium phase explosion and the relaxation of laser-induced stresses occurred in the central region with a high fluence.

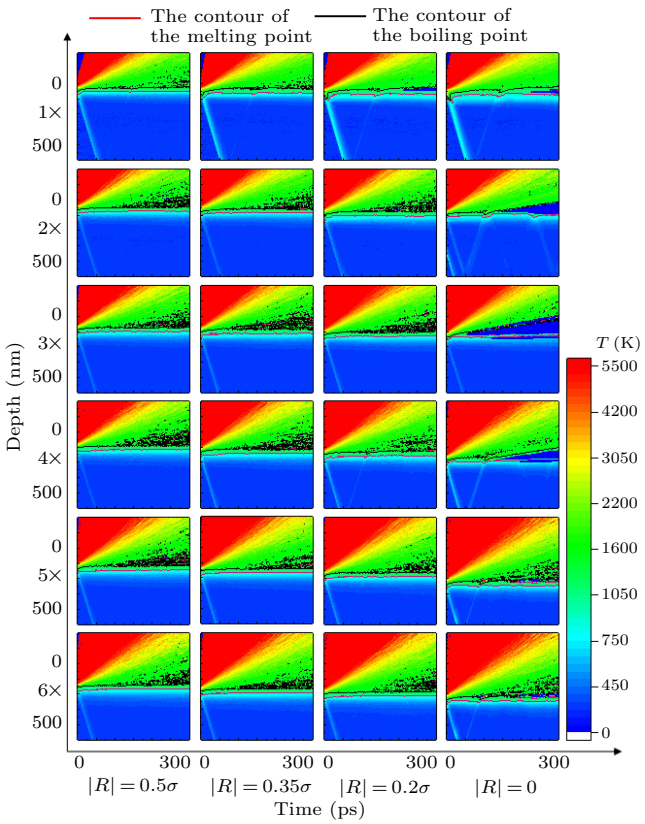


Fig. 14. Internal temperature field evolution of the Mg substrate under multi-pulse laser irradiation.

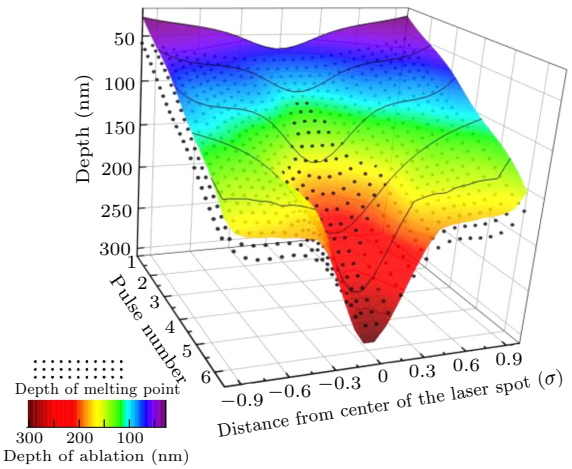


Fig. 15. The 3D surface of the melting depth and final ablation depth.

To verify the reliability of the evolution model obtained by simulation, a multi-pulse ablation experiment on the Mg substrate was designed and carried out. An industrial compact picosecond laser emitter at 355 nm (COMPILER 355, Passat Ltd., Vaughan, Canada) was used to ablate micro-holes on polished pure Mg surfaces. The construction of the optical path in the system was completed by Beijing G-star Optics Co, Ltd. Figure 16(a) illustrates the number of laser irradiations at different locations in a spot with a certain pulse overlap rate. According to this mechanism, the instability between pulses can be avoided by adjusting the scanning velocity. The scanning velocity v can be determined by the pulse number n, and we need

$$v = \frac{D}{n} \cdot f, \tag{9}$$

where D is the beam diameter, which is between 10 μm and 20 μm, and f is the repetition rate of the multi-pulse laser, which is fixed at 400 Hz. Since the laser spot radius is very small compared to the engineering component, it is often necessary to continuously move to achieve the desired machining effect. To avoid the effects of laser precision on the results and make the evolution process of the ablation crater consistent with the engineering application, scanning speeds of 100 μm/s, 120 μm/s and 150 μm/s were set, respectively, to achieve 60, 50 and 40 pulse superposition, and the duration of the laser was 0.2 s.

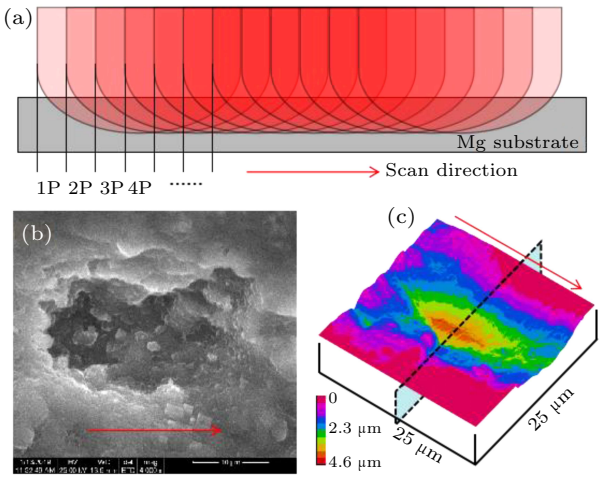


Fig. 16. The multi-pulse laser ablation experiment: (a) a schematic of the multi-pulse laser ablation; (b) an SEM view of the ablation crater; and (c) an AFM view of the ablation crater.

Figure 16(b) shows the scanning electron microscope (SEM) image of the ablation crater after 60 pulses were superimposed. Remelting and microparticle deposition can be observed at the bottom of the crater. To obtain more accurate depth information, an atomic force microscope (AFM) is used

to measure the contour of the crater. As shown in Fig. 16(c), the AFM range is 4.6 μm, and the maximum depth is measured in the middle section. Figure 17 shows the depth comparison of the experiments and simulations, which have a similar maximum depth. Due to the random nature of remelting and particle deposition, the experimental results exhibit fluctuations within a certain range. Nevertheless, these experimental results validate the validity of the MD simulation. This simulation method can be employed for the prediction of micromachining outcomes of intricate structures and for the selection of lasers with more optimal parameters.

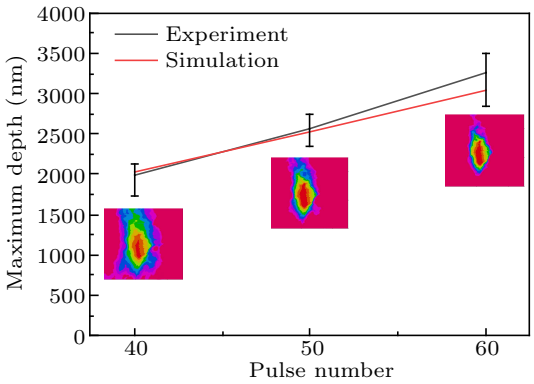


Fig. 17. Depth comparisons of the experiments and simulations.

4. Conclusion

MD simulation using LAMMPS is conducted to investigate the mechanism of laser ablation of Mg films and the evolution of craters under multi-pulse laser irradiation. These findings can serve as a basis for precision structure processing and surface texturing on Mg-based materials. The main conclusions are summarized as follows:

(1) The response of Mg film to lasers with varying pulse widths and energy fluences is obviously different. At low laser fluences, ablation mainly occurs on the substrate surface, which is manifested as energy absorption and ejection of surface atoms. However, at high laser fluences, not only the substrate surface but also the entire film is penetrated due to stress wave reflection and superposition.

(2) Due to the time distribution of the pulse laser energy, a long pulse width laser requires more energy to achieve the same ablation effect as a short pulse width laser. Moreover, comparison is made between the Mg[0001] and Mg[$10\bar{1}0$] substrates in response to laser irradiation, and it is found that Mg[0001] is more easily ablated than Mg[$10\bar{1}0$] due to its larger lattice constant and lower uniaxial strength. Through simulation of the response of single-crystal Mg films to laser irradiation with varying pulse widths and energy fluences, the fluence threshold that can penetrate the metal film is estimated, which is 200–25 mJ/cm^2 in Mg[$10\bar{1}0$] and 80–100 mJ/cm^2 in Mg[0001], respectively. Additionally, the penetration threshold decreases as the pulse width of the laser decreases.

(3) The simulation of multi-pulse laser ablation of Mg substrate was carried out and compared with the experiment, and the results were in good agreement. By observing the evolution of the crater profile with the number of pulses, a parabolic model from the initial surface to the deepest part was established. It found that not only does the crater depth increase linearly, but also the quadratic term and the constant term of the fitted crater profile curve increase linearly with the number of pulses. This model of crater evolution related to laser parameters is helpful for the prediction of crater morphology, which is important for understanding laser processing of magnesium-based materials.

References

[1] Li H N, Zhao Y J, Cao S, Chen H, Wu C, Qi H, Sun X, Wang H, Li C and Liu G 2021 *J. Mater. Process. Technol.* **295** 117149
[2] Zhao Y, Liu H G, Yu T B and Hong M H 2021 *Opt. Laser Technol.* **140** 107014
[3] Geng Z, Tong Z, Huang G, Zhong W, Cui C, Xu X and Jiang X 2022 *Int. J. Adv. Manuf. Tech.* **119** 5389
[4] Eisfeld E and Roth J 2018 *Adv. Opt. Technol.* **7** 189
[5] Markopoulos A P and Manolakos D E 2017 *Proc. Inst. Mech. Eng. Part B* **231** 415
[6] Tang G Q, Li B, Deng X L, Wang L, Zhu W J, Hu W Y and Gao F 2020 *Mech. Mater.* **148** 103479
[7] Kuo J K, Huang P H, Chien S K, Huang K Y and Chen K T 2018 *MATEC Web Conf. EDP Sciences* **167** 03011
[8] Wu C and Zhigilei L V 2014 *Appl. Phys. A* **114** 11
[9] Rethfeld B, Ivanov D S, Garcia M E and Anisimov S I 2017 *Phys. D: Appl. Phys.* **50** 193001
[10] Kharin A Y, Grigoryeva M S, Zavestovskaya I N and Timoshenko V Y 2021 *Laser Phys. Lett.* **18** 076001
[11] Miloshevsky A, Phillips M C, Harilal S S, Dressman P and Miloshevsky G 2017 *Phys. Rev. Mater.* **1** 063602
[12] Dey A and Pandey K M 2015 *Rev. Adv. Mater. Sci.* **42** 58
[13] Zhang X, Ma Q Y, Dai Y, Hu F P, Liu G, Xu Z Y, Wei G B, Xu T C, Zeng Q W and Xie W D 2018 *Appl. Surf. Sci.* **427** 897
[14] Pan Y C, Wu G Q, Huang Z, Li M Y, Ji S D and Zhang Z K 2017 *Surf. Coat. Technol.* **319** 309
[15] ElFaham M M, Okil M and Mostafa A M 2020 *J. Opt. Soc. Am. B* **37** 2620
[16] Yayoglu Y E, Gallant N D, Toomey R and Crane N B 2019 *International Mechanical Engineering Congress and Exposition*, November 11–14, 2019, Salt Lake City, UT, USA, p. V02BT02A034
[17] Plimpton S 1995 *J. Comput. Phys.* **117** 1
[18] Sun D Y, Mendelev M I, Becker C A and Kudin K 2006 *Phys. Rev. B* **73** 024116
[19] Sadao A 2012 *The handbook on optical constants of metals* (Singapore: World Scientific Publishing) p. 85
[20] Bulgakov A V and Bulgakova N M 1999 *Quantum Electron* **29** 433
[21] Schäfer C, Urbassek H M, Zhigilei L V and Garrison B 2002 *Comput. Mater. Sci.* **24** 421